THE JOURNAL OF
PHYSICAL CHEMISTRY
Letters

pubs.acs.org/JPCL Letter

Electronic Raman Scattering in Suspended Semiconducting Carbon Nanotube

Yuecong Hu, Shaochuang Chen, Xin Cong, Sida Sun, Jiang-bin Wu, Daqi Zhang, Feng Yang, Juan Yang,* Ping-Heng Tan, and Yan Li*

Cite This: *J. Phys. Chem. Lett.* 2020, 11, 10497−10503

ABSTRACT: The electronic Raman scattering (ERS) features of single-walled carbon nanotubes (SWNTs) can reveal a wealth of information about their electronic structures. Previously, the ERS processes have been exclusively reported in metallic SWNTs (M-SWNTs) and attributed to the inelastic scattering of photoexcited excitons by a continuum of low-energy electron−hole pairs near the Fermi level. Therefore, the ERS features have been thought to appear exclusively in M-SWNTs but not in semiconducting SWNTs (S-SWNTs), which are more desired in many application fields such as nanoelectronics and bioimaging. In this work, the experimental observation of the ERS features in suspended S-SWNTs is reported, the processes of which are accomplished via the available high-energy electron−hole pairs. The excitonic transition energies with an uncertainty in the order of ±1 meV can be directly obtained via the ERS spectra, compared to a typical uncertainty of ±10 meV in conventional electronic spectroscopies. The ERS features can facilitate further systematic studies on the properties of SWNT, both metallic and semiconducting, with defined chirality.

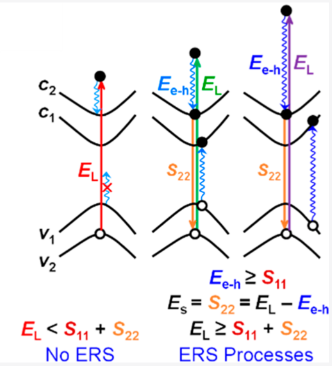

The electronic and phonon structures of the low-dimensional materials[1] are of vital importance in understanding their various properties. As a versatile tool, Raman spectroscopy has provided insight into those structures and the related properties.[2,3] Single-walled carbon nanotubes (SWNTs) are unique one-dimensional systems with abundant phonon[4,5] and electronic structures,[6,7] which can be probed by the phonon Raman scattering and the electronic Raman scattering (ERS), respectively. The phonon Raman processes involve the inelastic light scattering by various phonon modes and have been widely utilized in SWNT characterization.[8−15] The ERS processes, on the other hand, originate from the inelastic light scattering by a continuum of electron−hole (e−h) pairs. Consequently, the ERS processes can be resonantly enhanced at the excitonic transition energies (E_{ii}) of the SWNTs.[16−19] Due to the narrower bandwidth of the ERS features (30−50 meV) compared to the electronic transitions in regular electronic spectroscopies such as Rayleigh scattering[20,21] and optical absorption spectroscopies[22] (100−150 meV), the ERS spectra can provide direct and accurate information about the E_{ii} of SWNTs, which are of great importance to nanotube-related science and technology.

Previously, the ERS processes have been exclusively reported in metallic SWNTs (M-SWNTs) and attributed only to the low-energy e−h pairs created across their linear electronic sub-bands near the Fermi level.[16−19] Therefore, the ERS features have been thought to appear exclusively in M-SWNTs but not in semiconducting SWNTs (S-SWNTs), which are more desired in many application fields such as nanoelectronics[23−27] and bioimaging.[28−31] This has restricted the understanding to the fundamental processes of ERS and limited their potential applications.

In this work, we extend the ERS processes to all types of SWNTs and show that the ERS features are not only applicable to M-SWNTs but also can be observed in S-SWNTs. Our results support that the ERS processes are accomplished by a continuum of e−h pairs across the electronic sub-bands, both low-energy and high-energy. We report that the E_{ii} (M_{ii} for M-SWNTs and S_{ii} for S-SWNTs) with an uncertainty in the order of ±1 meV can be directly obtained via the ERS spectra, compared to a typical uncertainty of ±10 meV in conventional electronic spectroscopies.[20−22] The ERS features, which can be observed up to ~9000 cm^{-1} (~1.1 eV) away from the excitation laser energy, reveal a wealth of information about the electronic structures of the SWNTs that can facilitate further systematic studies.

Comparing the electronic band structure of S-SWNTs to that of the M-SWNTs, it can be found that the major differnce lies in the absence of a pair of linear electronic sub-bands arising from the gapless dispersion near the K point. Therefore, S-SWNTs do not possess the low-energy e−h pairs ($E_{e-h} < S_{11}$) across the linear electronic sub-bands but have high-

Received: November 5, 2020
Accepted: December 1, 2020

https://dx.doi.org/10.1021/acs.jpclett.0c03320

energy e−h pairs with energy above S_{11} ($E_{\mathrm{e-h}} \geq S_{11}$). Similar to the ERS processes in M-SWNTs accomplished by a continuum of low-energy e−h pairs, the ERS processes in S-SWNTs can be accomplished by a continuum of those high-energy e−h pairs. The electronic band structures of the first-order intravalley interactions of the ERS processes in S-SWNTs are schematically shown in Figure 1a, and the corresponding density of states diagram is given in Figure 1b. If the excitation laser energy (E_L) is set to be slightly higher than an E_{ii}, the ERS spectra can only be observed for M-SWNTs but not for S-SWNTs because only the low-energy e−h pairs matching the corresponding energy difference of $E_L - E_{ii}$ in M-SWNTs can contribute to this ERS process. No such low-energy e−h pairs are present in S-SWNTs to accomplish this ERS process. However, if E_L is set to be sufficiently high so that the energy difference of $E_L - E_{ii}$ can match those available high-energy e−h pairs in S-SWNTs, we do expect to observe the ERS spectra in S-SWNTs that can be accomplished by the continuum of those high-energy e−h pairs. For instance, if $E_L \geq S_{11} + S_{22}$ is satisfied, an ERS feature can be anticipated at S_{22} involving in the light scattering by the continuum of e−h pairs near $E_{\mathrm{e-h}} = E_L - S_{22} \geq S_{11}$. Similar ERS features are expected at higher S_{ii} with an E_L satisfying $E_L \geq S_{11} + S_{ii}$.

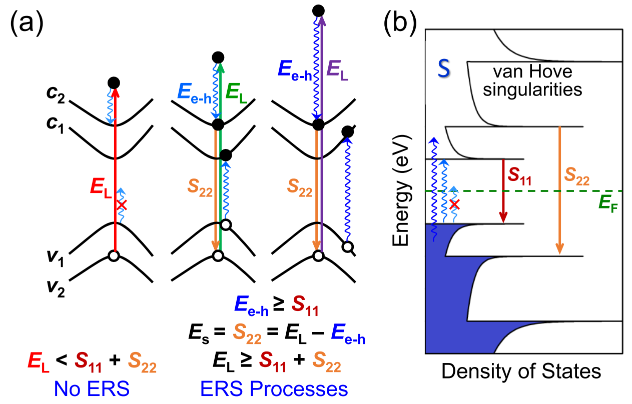

Figure 1. Schematics of the ERS processes in S-SWNTs. (a) Electronic band structures of the first-order intravalley interactions of the ERS processes at different excitation lasers in an S-SWNT. Only high-energy e−h pairs with $E_{\mathrm{e-h}} \geq S_{11}$ are available in S-SWNTs. If $E_L < S_{11} + S_{22}$, no ERS is expected due to the absence of the low-energy e−h pairs matching the corresponding energy difference of $E_L - E_{22}$. When $E_L \geq S_{11} + S_{22}$ is satisfied, the ERS processes are expected at S_{22} by the continuum of e−h pairs near $E_{\mathrm{e-h}} = E_L - S_{22} \geq S_{11}$. E_L, E_s, and $E_{\mathrm{e-h}}$ represent the energies of laser, scattered photon, and e−h pair, respectively. (b) Density of states diagram of this S-SWNT with the corresponding e−h pairs and electronic transitions.

The individual suspended SWNTs grown over the open slits of SiO_2/Si substrate with Co catalysts via chemical vapor deposition (CVD)[18,32] were used in this study. Figure 2a shows the Raman spectrum of a suspended S-SWNT at 532 nm excitation in a wide range of 100−7500 $\mathrm{cm^{-1}}$. According to the radial breathing mode (RBM) at 187 $\mathrm{cm^{-1}}$ observed with both 532 and 785 nm lasers and the photoluminescence (PL) peak at 0.799 eV with the 785 nm laser (Figure 2b), we can determine its chirality as (15,2) using the (n,m) assignment program we have previously proposed (www.chem.pku.edu.cn/cnt_assign).[33] From the (n,m) calculator we launched on the same Web site, we calculate that S_{11} = 0.803 eV and S_{22} = 1.522 eV for an air-suspended (15,2) nanotube. The summation of $S_{11} + S_{22}$ = 2.325 eV is slightly lower than the 532 nm laser energy (E_L = 2.330 eV). Therefore, we expect an ERS feature at $E_{\mathrm{e-h}} = E_L - S_{22}$ = 0.808 eV, which corresponds to ~6520 $\mathrm{cm^{-1}}$. Experimentally, we observe two features in the 6000−7500 $\mathrm{cm^{-1}}$ region: a phonon peak that can be assigned to the G+4D combinational mode at 6802 $\mathrm{cm^{-1}}$ with a full width at half-maximum (fwhm) of 99 $\mathrm{cm^{-1}}$ (12 meV), and an ERS band at 6587 $\mathrm{cm^{-1}}$ with a fwhm of 291 $\mathrm{cm^{-1}}$ (36 meV). The experimental spectra agree with our expectation for ERS, with a slight differnece of only 67 $\mathrm{cm^{-1}}$ (8 meV) arising from the environmental effects including adsorbed gas molecules, bundling effect, amorphous carbon coating, etc. Note that the combinational mode G+4D show significantly enhanced Raman intensity compared to the combinational modes G+2D and 2G+2D. This can be explained by the scattered resonance condition[7,11] of its scattered photon energy with the S_{22}. Considering a spectral resolution of 0.5 meV (~4 $\mathrm{cm^{-1}}$ with a 300 grooves/mm grating), an error introduced by random noise of 0.2 meV, and a spectral fitting error with different initial parameters of 1.3 meV, we estimate that the error in determining S_{22} is ±1 meV for a single ERS spectrum. Therefore, we calculate an accurate value of S_{22} = 1.513 eV from the ERS feature for this particular nanotube. Together with what we have reported previously for M-SWNTs,[19] we conclude that E_{ii} with an uncertainty in the order of ±1 meV can be directly obtained via the ERS features for all types of SWNTs, both metallic and semiconducting. Even when the environmental effects are taken into consideration, the uncertainty in determining E_{ii} is still on the order of ±10 meV, which is significantly better than the ±100 meV uncertainty from Raman excitation profile[34−36] or from the conventional electronic spectroscopies such as Rayleigh scattering[37,38] and transmission spectroscopies.[39]

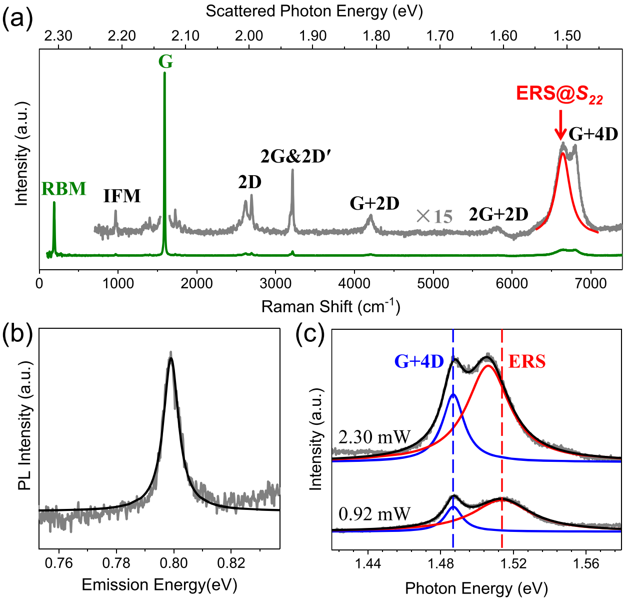

Figure 2. Raman and PL spectra of a suspended (15,2) nanotube. (a) Wide range Raman spectra at 532 nm excitation, showing various phonon peaks and an ERS band corresponding to S_{22}. (b) PL spectra at 785 nm excitation. (c) Raman spectra at different powers of the 532 nm laser. The ERS band, the phonon peaks, and the PL peak are fitted with a Lorentzian line shape.

We intentionally heat this suspended (15,2) nanotube with different powers of the 532 nm laser (Figure 2c) to reveal how temperature changes have affected both the ERS feature and the phonon peak. Compared to the spectrum collected at a low laser power (0.92 mW) showing a negligible laser heating effect, at an increased laser power (2.30 mW) the ERS feature red shifts due to the thermal expansion of the nanotube and the consequently decreased transition energies whereas the G +4D phonon peak, as well as all other phone peaks (Figure S1, Supporting Information), remains nearly unchanged. A further increase in the laser power leads to burning down of this nanotube. The laser heating effect on the ERS features of S-SWNTs are in good agreement with our previous data on the ERS features of M-SWNTs.[18] We find that suspended S-SWNTs are more vulnerable to increased laser powers than suspended M-SWNTs, which can be explained by their poorer thermal conductivity than M-SWNTs.

We use five different lasers (E_L = 1.579, 1.959, 2.330, 2.412, and 2.540 eV) to verify this ERS feature (Figure 3a). If our understanding of the ERS process via the high-energy e−h pairs is correct, we expect to observe this ERS feature only with E_L = 2.330, 2.412, and 2.540 eV, which satisfy the condition of $E_L \geq S_{11} + S_{22}$, but not with E_L = 1.579 and 1.959 eV, which do not satisfy the condition of $E_L \geq S_{11} + S_{22}$. Experimentally, we observe various phonon Raman features of this nanotube with E_L = 1.579 eV. However, we do not observe any ERS feature at $E_L - S_{22}$ = 0.066 eV, which corresponds to ~530 cm^{-1} (marked by a red arrow in the top panel of Figure 3a). Similarly, no ERS feature is observed at $E_L - S_{22}$ = 0.446 eV or ~3600 cm^{-1} with E_L = 1.959 eV. We do observe weak but definite ERS features with the three higher energy lasers. With E_L = 2.412 eV, the ERS feature is expected at $E_L - S_{22}$ = 0.899 eV or ~7250 cm^{-1} and is observed at 7320 cm^{-1} (fwhm = 210 cm^{-1}). With E_L = 2.540 eV, the ERS feature is expected at $E_L - S_{22}$ = 1.027 eV or ~8280 cm^{-1} and is observed at 8317 cm^{-1} (fwhm = 310 cm^{-1}).

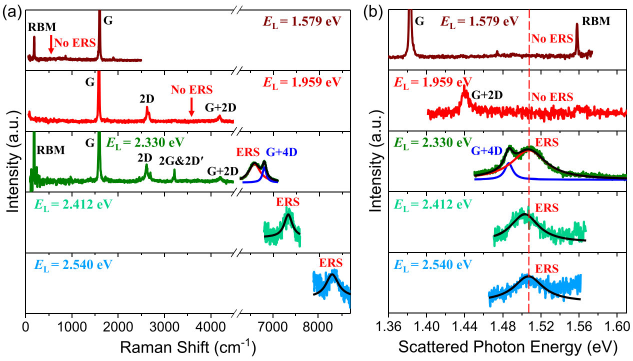

Figure 3. Raman spectra and the ERS feature of a suspended (15,2) nanotube at different excitation lasers (E_L = 1.579, 1.959, 2.330, 2.412, and 2.540 eV) with respect to (a) the Raman shift and (b) scattered photon energy. No ERS is observed with E_L = 1.579 and 1.959 eV as the condition of $E_L \geq S_{11} + S_{22}$ = 2.325 eV is not satisfied. The ERS feature is observed at S_{22} with E_L = 2.330, 2.412, and 2.540 eV since the condition of $E_L \geq S_{11} + S_{22}$ = 2.325 eV is satisfied.

Converting the Raman shifts to the corresponding scattered photon energy (Figure 3b), all the ERS features remain centered around ~1.51 eV regardless of E_L, which provides direct information about the S_{22} of (15,2). The slightly shifted S_{22} values (less than 10 meV) may arise from the temperature-induced thermal effect[40,41] and the photoexcited carrier induced Coulomb screening.[17,42] The gas molecules adsorbed on the SWNT walls[43,44] may desorb at different experimental conditions including ambient temperature variation and laser heating effect. The Coulomb interaction induced by photoexcited carriers could cause a significant band gap renormalization effect, which alters the excitonic transition energies of SWNTs.[42] No phonon peak is observed near the ERS features with E_L = 2.412 or 2.540 eV due to the absence of phonon modes in scattered resonance condition with the S_{22} at these two excitations. More importantly, these results rule out high-energy PL as a possible interpretation for the feature around ~1.51 eV. Although both are expected to appear at S_{22}, high-energy PL, which results from the recombination of excitons at S_{22} after relaxation, should occur at excitation energies higher than S_{22} ($E_L \geq S_{22}$), whereas ERS is anticipated at excitation energies higher than $S_{11} + S_{22}$ ($E_L \geq S_{11} + S_{22}$). As shown in Figure 3, when exciting a suspended (15,2) nanotube with E_L = 1.579 eV, which is higher than S_{22} = 1.522 eV but lower than $S_{11} + S_{22}$ = 2.325 eV, we do not observe this feature at S_{22}. This spectrum clearly demonstrates that this feature arises from ERS rather than high-energy PL.

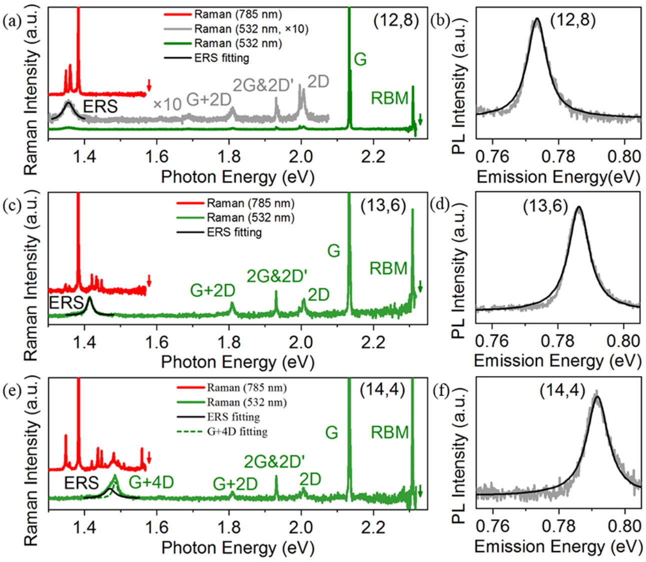

Figure 4. Raman and ERS features (a, c, e) and PL spectra (b, d, f) of suspended (12,8), (13,6), and (14,4) nanotubes in the $2n + m = 32$ family at 532 (green) and 785 (red) nm excitations. The ERS bands and the PL peaks are fitted with a Lorentzian line shape. The arrows indicate the energies of the corresponding excitation laser lines.

We also observe the ERS features of the other chiralities in the $2n + m = 32$ family, to which (15,2) belongs. Figure 4 shows the ERS and PL spectra of suspended (14,4), (13,6), and (12,8) nanotubes and Table 1 summarizes all the information. When multiple nanotubes of the same chiralities are found, we use the one with the highest transition energy, which is most likely to be an individual tube without the bundling effect. The ERS data of other nanotubes are given in Figure S2 and listed in Table S1. In the $2n + m = 32$ family, S_{22} decreases with increasing θ.[10,45] The condition of $E_L \geq S_{11} + S_{22}$ is satisfied with E_L = 2.330 eV but not with E_L = 1.579 eV for all the chiralities in this family. Therefore, we expect to observe continuously red-shifted ERS features (or continuously upshifted Raman shifts for the ERS features) with increasing θ at E_L = 2.330 eV but no ERS feature at E_L = 1.579 eV. Experimentally, we do not observe any ERS feature with

Table 1. Transition Energies, ERS Features, and PL Peak of the Suspended Chiral Nanotubes in the $2n + m = 32$ Family

(*n*,*m*)	S_{11}[a] [eV]	S_{22}[a] [eV]	$S_{11} + S_{22}$ [eV]	E_L [eV]	RBM [cm^{-1}]	ERS expected [eV]	ERS observed [eV]	ΔS_{22} [eV]	PL observed [eV]	ΔS_{11} [eV]
(15,2)	0.803	1.522	2.325	1.579	187	no ERS	none		0.799	−0.004
				1.959	none	no ERS	none			
				2.330	187	1.522	1.513	−0.009		
				2.412	none	1.522	1.504	−0.018		
				2.540	none	1.522	1.509	−0.013		
(14,4)	0.797	1.485	2.282	1.579	180	no ERS	none		0.792	−0.005
				2.330	180	1.485	1.470	−0.015		
(13,6)	0.785	1.431	2.216	1.579	none	no ERS	none		0.786	0.001
				2.330	178	1.431	1.415	−0.016		
(12,8)	0.769	1.365	2.134	1.579	none	no ERS	none		0.774	0.005
				2.330	170	1.365	1.356	−0.009		

[a] Calculated using the (*n*,*m*) calculator on www.chem.pku.edu.cn/cnt_assign.

the 1.579 eV laser for all the chiralities. We observe the ERS features at 1.470, 1.415, and 1.356 eV for (14,4), (13,6), and (12,8), respectively, with the 2.330 eV laser. The combinational mode G+4D also appears in (14,4) due to the scattered resonance but is located at the higher energy side of the ERS. This combinational mode does not show in (13,6) and (12,8) because it is out of the scattered resonance. In addition, although no ERS feature is observed at E_L = 1.579 eV, the relative phonon peak intensity variations match the corresponding scattered resonance with S_{22}. For instance, (13,6) shows a strong intermediate frequency mode (IFM, 1000−1200 cm^{-1}) because the scattered photon energy of IFM is close to its S_{22} (~1320 cm^{-1}) whereas intense M-band (~1750 cm^{-1}) and iTOLA (~1950 cm^{-1}) modes are present for (12,8) with an upshifted S_{22} value (~1800 cm^{-1}) compared to that for (13,6). Figure 5 shows the data for all four nanotubes in the bilayer plot that we have developed previously.[33] From the S_{11} and S_{22} values, we can calculate the splitting $S_{22} - S_{11}$ and average $(S_{22} + S_{11})/2$ values, which are indicated by the red squares. Blue diamonds indicate the splitting vs the RBM value. These data agree with the corresponding chiralities in the bilayer plot. All blue diamonds are located to the left of the corresponding red squares, suggesting that all these four nanotubes are individual tubes.[33]

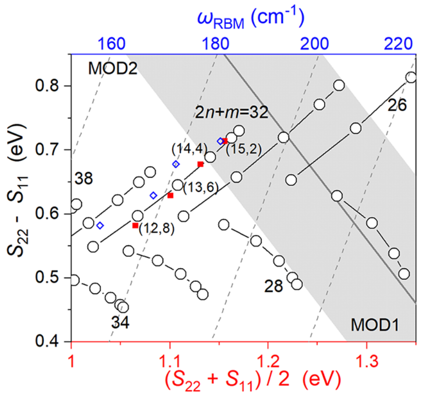

Figure 5. Data of four suspended (15,2), (14,4), (13,6), and (14,8) nanotubes shown in the bilayer plot. Red squares are in splitting $S_{22} - S_{11}$ vs average $(S_{22} + S_{11})/2$ scale, and blue diamonds are in splitting $S_{22} - S_{11}$ vs ω_{RBM} scale.

If the condition of $E_L \geq 2\ S_{11}$ is satisfied, we expect to observe an ERS feature at S_{11} by the continuum of e−h pairs near $E_{e-h} = E_L - S_{11} \geq S_{11}$. However, this feature could not be distinguished from the PL peak at ambient conditions and is not the focus of this work. We speculate that two possible methods can be used to resolve this ERS feature from the PL peak. One is by time-resolved measurements since the exciton relaxation that PL involves is a slower process than the ERS process.[46] The other is by low temperature experiments because PL corresponds to the transition from the bright excitonic states with slightly higher energy than the dark excitonic states that can also be accessed by the ERS process.[47]

In conclusion, we have shown that the ERS features can be observed for S-SWNTs, which are accomplished via the available high-energy e−h pairs with $E_{e-h} \geq S_{11}$. When the condition of $E_L \geq S_{11} + S_{22}$ is satisfied, the ERS band is observed at the corresponding S_{22} via those high-energy e−h pairs ($E_{e-h} = E_L - S_{22} \geq S_{11}$). The transition energies can be determined with an uncertainty on the order of ±1 meV for a single spectrum and on the order of ±10 meV taking into account the environmental effects. The ERS approach can facilitate the precise assignment of SWNT chirality and further systematic studies on the properties of SWNT, both metallic and semiconducting, with defined chirality.

■ EXPERIMENTAL SECTION

Sample Preparation. SiO_2/Si wafers with open slits (typical width of 20, 40, and 60 μm) were used as the substrates. The growth of SWNTs was carried out by a fast-heating CVD process. Typically, 0.1 mmol L^{-1} $Co(CH_3COO)_2$ was used as the catalyst precursor. The substrate was placed into a quartz tube (1 in. in diameter) and calcined at 500 °C in air for 5 min. Then the quartz tube was pulled out of the heating zone of the furnace, and the furnace temperature was ramped up to 1000 °C under 300 standard-state cubic centimeters per minute (sccm) Ar in 8 min. When the temperature was stabilized, the gas was switched to 135 sccm Ar carrying ethanol vapor (25 °C) and 25 sccm H_2. Then the quartz tube was slid into the heating zone of the furnace, and the temperature was set to 950 °C. After growing at 950 °C for 3−5 min, the ethanol supply was stopped, and the system was cooled to room temperature under Ar and H_2.

Raman Measurements. Raman measurements were performed on a Horiba Jobin-Yvon LabRAM ARAMIS system with excitation wavelengths of 532 nm (2.330 eV), 633 nm (1.959 eV), and 785 nm (1.579 eV), and a Horiba Jobin-Yvon HR800 system with excitation wavelengths of 488 nm (2.540 eV) and 514 nm (2.412 eV). The laser polarization was set to be parallel to the orientation of the nanotubes. Stokes Raman spectra were acquired with edge filters cutting at 50 cm^{-1}. Both 300 and 600 grooves/mm gratings were used, giving a spectral resolution of about 4 and 2 cm^{-1}. The Raman shift was calibrated with respect to the silicon peak at 521 cm^{-1} and a series of neon lines. The laser power was controlled under 1 mW to avoid laser heating effect, unless higher laser powers were intentionally used for some experiments. A 100× air objective was used, and the laser spot was about 1 μm in diameter. The accumulation time was 200, 300, and 600 s for different spectra in order to achieve a proper signal-to-noise ratio. The background signal was acquired on the blank substrate under exactly the same conditions and was subtracted from all Raman spectra.

PL Measurements. PL measurements were performed on a Horiba Jobin-Yvon LabRAM ARAMIS system with excitation wavelengths of 532 nm (2.330 eV), 633 nm (1.959 eV), and 785 nm (1.579 eV). Both 300 and 600 grooves/mm gratings were used. A 100× air objective was used, and the laser spot was about 1 μm in diameter. The accumulation time was several tens of seconds for different spectra in order to achieve a proper signal-to-noise ratio.

■ ASSOCIATED CONTENT

Supporting Information

The Supporting Information is available free of charge at https://pubs.acs.org/doi/10.1021/acs.jpclett.0c03320.

> Error analysis for ERS spectra, laser heating effect, Raman and PL spectra, ESR features, and table of transition energies, ERS features, and PL peaks (PDF)

■ AUTHOR INFORMATION

Corresponding Authors

Juan Yang − *Beijing National Laboratory for Molecular Sciences, Key Laboratory for the Physics and Chemistry of Nanodevices, State Key Laboratory of Rare Earth Materials Chemistry and Applications, College of Chemistry and Molecular Engineering, Peking University, Beijing 100871, China;* orcid.org/0000-0001-5502-9351; Email: yang_juan@pku.edu.cn

Yan Li − *Beijing National Laboratory for Molecular Sciences, Key Laboratory for the Physics and Chemistry of Nanodevices, State Key Laboratory of Rare Earth Materials Chemistry and Applications, College of Chemistry and Molecular Engineering, Peking University, Beijing 100871, China;* orcid.org/0000-0002-3828-8340; Email: yanli@pku.edu.cn

Authors

Yuecong Hu − *Beijing National Laboratory for Molecular Sciences, Key Laboratory for the Physics and Chemistry of Nanodevices, State Key Laboratory of Rare Earth Materials Chemistry and Applications, College of Chemistry and Molecular Engineering, Peking University, Beijing 100871, China*

Shaochuang Chen − *Beijing National Laboratory for Molecular Sciences, Key Laboratory for the Physics and Chemistry of Nanodevices, State Key Laboratory of Rare Earth Materials Chemistry and Applications, College of Chemistry and Molecular Engineering, Peking University, Beijing 100871, China*

Xin Cong − *State Key Laboratory of Superlattices and Microstructures, Institute of Semiconductors, Chinese Academy of Sciences, Beijing 100083, China*

Sida Sun − *Beijing National Laboratory for Molecular Sciences, Key Laboratory for the Physics and Chemistry of Nanodevices, State Key Laboratory of Rare Earth Materials Chemistry and Applications, College of Chemistry and Molecular Engineering, Peking University, Beijing 100871, China*

Jiang-bin Wu − *State Key Laboratory of Superlattices and Microstructures, Institute of Semiconductors, Chinese Academy of Sciences, Beijing 100083, China*

Daqi Zhang − *Beijing National Laboratory for Molecular Sciences, Key Laboratory for the Physics and Chemistry of Nanodevices, State Key Laboratory of Rare Earth Materials Chemistry and Applications, College of Chemistry and Molecular Engineering, Peking University, Beijing 100871, China*

Feng Yang − *Beijing National Laboratory for Molecular Sciences, Key Laboratory for the Physics and Chemistry of Nanodevices, State Key Laboratory of Rare Earth Materials Chemistry and Applications, College of Chemistry and Molecular Engineering, Peking University, Beijing 100871, China;* orcid.org/0000-0002-3637-814X

Ping-Heng Tan − *State Key Laboratory of Superlattices and Microstructures, Institute of Semiconductors, Chinese Academy of Sciences, Beijing 100083, China;* orcid.org/0000-0001-6575-1516

Complete contact information is available at: https://pubs.acs.org/10.1021/acs.jpclett.0c03320

Author Contributions

Y. C. Hu and S. C. Chen contributed equally to this work.

Notes

The authors declare no competing financial interest.

■ ACKNOWLEDGMENTS

The authors acknowledge the National Key Research and Development Program of China (Grants 2016YFA0201904 and 2016YFA0301204), National Natural Science Foundation of China (Grants 21873008, 21631002, and 11874350), and Beijing National Laboratory for Molecular Sciences (BNLMS-CXTD-202001).

■ REFERENCES

(1) Pinczuk, A.; Abstreiter, G. *Light Scattering in Solids V*; Springer-Verlag: Berlin, 1989.

(2) Jorio, A.; Saito, R.; Dresselhaus, G.; Dresselhaus, M. S. *Raman Spectroscopy in Graphene Related Systems*; Wiley-VCH: Singapore, 2011.

(3) Wu, J. B.; Lin, M. L.; Cong, X.; Liu, H. N.; Tan, P. H. Raman spectroscopy of graphene-based materials and its applications in related devices. *Chem. Soc. Rev.* **2018**, 47, 1822−1873.

(4) Jiang, J.; Saito, R.; Samsonidze, G. G.; Chou, S. G.; Jorio, A.; Dresselhaus, G.; Dresselhaus, M. S. Electron-phonon matrix elements in single-wall carbon nanotubes. *Phys. Rev. B: Condens. Matter Mater. Phys.* **2005**, 72, 235408.

(5) Lim, Y. S.; Nugraha, A. R. T.; Cho, S. J.; Noh, M. Y.; Yoon, E. J.; Liu, H. P.; Kim, J. H.; Telg, H.; Haroz, E. H.; Sanders, G. D.; Baik, S. H.; Kataura, H.; Doorn, S. K.; Stanton, C. J.; Saito, R.; Kono, J.; Joo, T. Ultrafast Generation of Fundamental and Multiple-Order Phonon Excitations in Highly Enriched (6,5) Single-Wall Carbon Nanotubes. *Nano Lett.* **2014**, *14*, 1426−1432.

(6) Samsonidze, G. G.; Saito, R.; Jorio, A.; Pimenta, M. A.; Souza, A. G.; Gruneis, A.; Dresselhaus, G.; Dresselhaus, M. S. The concept of cutting lines in carbon nanotube science. *J. Nanosci. Nanotechnol.* **2003**, *3*, 431−458.

(7) Dresselhaus, M. S.; Dresselhaus, G.; Saito, R.; Jorio, A. Raman spectroscopy of carbon nanotubes. *Phys. Rep.* **2005**, *409*, 47−99.

(8) Rao, A. M.; Richter, E.; Bandow, S.; Chase, B.; Eklund, P. C.; Williams, K. A.; Fang, S.; Subbaswamy, K. R.; Menon, M.; Thess, A.; Smalley, R. E.; Dresselhaus, G.; Dresselhaus, M. S. Diameter-selective Raman scattering from vibrational modes in carbon nanotubes. *Science* **1997**, *275*, 187−191.

(9) Jorio, A.; Santos, A. P.; Ribeiro, H. B.; Fantini, C.; Souza, M.; Vieira, J. P. M.; Furtado, C. A.; Jiang, J.; Saito, R.; Balzano, L.; Resasco, D. E.; Pimenta, M. A. Quantifying carbon-nanotube species with resonance Raman scattering. *Phys. Rev. B: Condens. Matter Mater. Phys.* **2005**, *72*, 075207.

(10) Araujo, P. T.; Doorn, S. K.; Kilina, S.; Tretiak, S.; Einarsson, E.; Maruyama, S.; Chacham, H.; Pimenta, M. A.; Jorio, A. Third and fourth optical transitions in semiconducting carbon nanotubes. *Phys. Rev. Lett.* **2007**, *98*, 067401.

(11) Saito, R.; Hofmann, M.; Dresselhaus, G.; Jorio, A.; Dresselhaus, M. S. Raman spectroscopy of graphene and carbon nanotubes. *Adv. Phys.* **2011**, *60*, 413−550.

(12) Zhang, D. Q.; Yang, J.; Li, Y. Spectroscopic Characterization of the Chiral Structure of Individual Single-Walled Carbon Nanotubes and the Edge Structure of Isolated Graphene Nanoribbons. *Small* **2013**, *9*, 1284−1304.

(13) Zhao, Q. C.; Zhang, J. Characterizing the Chiral Index of a Single-Walled Carbon Nanotube. *Small* **2014**, *10*, 4586−4605.

(14) Inaba, T.; Tanaka, Y.; Konabe, S.; Homma, Y. Effects of Chirality and Defect Density on the Intermediate Frequency Raman Modes of Individually Suspended Single-Walled Carbon Nanotubes. *J. Phys. Chem. C* **2018**, *122*, 9184−9190.

(15) Yang, F.; Wang, M.; Zhang, D.; Yang, J.; Zheng, M.; Li, Y. Chirality Pure Carbon Nanotubes: Growth, Sorting, and Characterization. *Chem. Rev.* **2020**, *120*, 2693−2758.

(16) Farhat, H.; Berciaud, S.; Kalbac, M.; Saito, R.; Heinz, T. F.; Dresselhaus, M. S.; Kong, J. Observation of Electronic Raman Scattering in Metallic Carbon Nanotubes. *Phys. Rev. Lett.* **2011**, *107*, 157401.

(17) Hasdeo, E. H.; Nugraha, A. R. T.; Sato, K.; Dresselhaus, M. S.; Saito, R. Electronic Raman scattering and the Fano resonance in metallic carbon nanotubes. *Phys. Rev. B: Condens. Matter Mater. Phys.* **2013**, *88*, 115107.

(18) Zhang, D. Q.; Yang, J.; Hasdeo, E. H.; Liu, C.; Liu, K. H.; Saito, R.; Li, Y. Multiple electronic Raman scatterings in a single metallic carbon nanotube. *Phys. Rev. B: Condens. Matter Mater. Phys.* **2016**, *93*, 245428.

(19) Zhang, D. Q.; Yang, J.; Li, M. H.; Li, Y. (n, m) Assignments of Metallic Single-Walled Carbon Nanotubes by Raman Spectroscopy: The Importance of Electronic Raman Scattering. *ACS Nano* **2016**, *10*, 10789−10797.

(20) Liu, K. H.; Deslippe, J.; Xiao, F. J.; Capaz, R. B.; Hong, X. P.; Aloni, S.; Zettl, A.; Wang, W. L.; Bai, X. D.; Louie, S. G.; Wang, E. G.; Wang, F. An atlas of carbon nanotube optical transitions. *Nat. Nanotechnol.* **2012**, *7*, 325−329.

(21) Zhao, S. H.; Kitagawa, T.; Miyauchi, Y.; Matsuda, K.; Shinohara, H.; Kitaura, R. Rayleigh scattering studies on inter-layer interactions in structure-defined individual double-wall carbon nanotubes. *Nano Res.* **2014**, *7*, 1548−1555.

(22) Liu, K. H.; Hong, X. P.; Choi, S.; Jin, C. H.; Capaz, R. B.; Kim, J.; Wang, W. L.; Bai, X. D.; Louie, S. G.; Wang, E. G.; Wang, F. Systematic determination of absolute absorption cross-section of individual carbon nanotubes. *Proc. Natl. Acad. Sci. U. S. A.* **2014**, *111*, 7564−7569.

(23) Javey, A.; Guo, J.; Wang, Q.; Lundstrom, M.; Dai, H. J. Ballistic carbon nanotube field-effect transistors. *Nature* **2003**, *424*, 654−657.

(24) Liu, L.; Han, J.; Xu, L.; Zhou, J.; Zhao, C.; Ding, S.; Shi, H.; Xiao, M.; Ding, L.; Ma, Z.; Jin, C.; Zhang, Z.; Peng, L. M. Aligned, high-density semiconducting carbon nanotube arrays for high-performance electronics. *Science* **2020**, *368*, 850−856.

(25) Qiu, S.; Wu, K.; Gao, B.; Li, L.; Jin, H.; Li, Q. Solution-Processing of High-Purity Semiconducting Single-Walled Carbon Nanotubes for Electronics Devices. *Adv. Mater.* **2019**, *31*, No. e1800750.

(26) Peng, L.-M.; Zhang, Z.; Qiu, C. Carbon nanotube digital electronics. *Nat. Electron.* **2019**, *2*, 499−505.

(27) Hills, G.; Lau, C.; Wright, A.; Fuller, S.; Bishop, M. D.; Srimani, T.; Kanhaiya, P.; Ho, R.; Amer, A.; Stein, Y.; Murphy, D.; Arvind; Chandrakasan, A.; Shulaker, M. M. Modern microprocessor built from complementary carbon nanotube transistors. *Nature* **2019**, *572*, 595−602.

(28) Yomogida, Y.; Tanaka, T.; Zhang, M. F.; Yudasaka, M.; Wei, X. J.; Kataura, H. Industrial-scale separation of high-purity single-chirality single-wall carbon nanotubes for biological imaging. *Nat. Commun.* **2016**, *7*, 12056.

(29) Cui, X.; Xu, S.; Wang, X.; Chen, C. The nano-bio interaction and biomedical applications of carbon nanomaterials. *Carbon* **2018**, *138*, 436−450.

(30) Wang, H.; Mu, X.; Yang, J.; Liang, Y.; Zhang, X.-D.; Ming, D. Brain imaging with near-infrared fluorophores. *Coord. Chem. Rev.* **2019**, *380*, 550−571.

(31) Kenry; Duan, Y.; Liu, B. Recent Advances of Optical Imaging in the Second Near-Infrared Window. *Adv. Mater.* **2018**, *30*, No. e1802394.

(32) Zhou, W.; Han, Z.; Wang, J.; Zhang, Y.; Jin, Z.; Sun, X.; Zhang, Y.; Yan, C.; Li, Y. Copper catalyzing growth of single-walled carbon nanotubes on substrates. *Nano Lett.* **2006**, *6*, 2987−2990.

(33) Yang, J.; Zhang, D. Q.; Hu, Y. C.; Xia, C. M. Y.; Sun, S. D.; Li, Y. Bilayer Plots for Accurately Determining the Chirality of Single-Walled Carbon Nanotubes Under Complex Environments. *ACS Nano* **2017**, *11*, 10509−10518.

(34) Yin, Y.; Swan, A. K.; Walsh, A. G.; Vamivakas, A. N.; Cronin, S. B.; Stolyarov, A. M.; Tinkham, M.; Bacsa, W.; Unlu, M. S.; Goldberg, B. B. Tunable Resonant Raman Scattering From Singly Resonant Single Wall Carbon Nanotubes. *IEEE J. Sel. Top. Quantum Electron.* **2006**, *12*, 1083−1090.

(35) Doorn, S. K.; Araujo, P. T.; Hata, K.; Jorio, A. Excitons and exciton-phonon coupling in metallic single-walled carbon nanotubes: Resonance Raman spectroscopy. *Phys. Rev. B: Condens. Matter Mater. Phys.* **2008**, *78*, 165408.

(36) Hsieh, Y.-P.; Hofmann, M.; Farhat, H.; Barros, E. B.; Kalbac, M.; Kong, J.; Liang, C.-T.; Chen, Y.-F.; Dresselhaus, M. S. Chiral angle dependence of resonance window widths in (2n+m) families of single-walled carbon nanotubes. *Appl. Phys. Lett.* **2010**, *96*, 103118.

(37) Liu, K.; Deslippe, J.; Xiao, F.; Capaz, R. B.; Hong, X.; Aloni, S.; Zettl, A.; Wang, W.; Bai, X.; Louie, S. G.; Wang, E.; Wang, F. An atlas of carbon nanotube optical transitions. *Nat. Nanotechnol.* **2012**, *7*, 325−329.

(38) Zhao, S.; Kitagawa, T.; Miyauchi, Y.; Matsuda, K.; Shinohara, H.; Kitaura, R. Rayleigh scattering studies on inter-layer interactions in structure-defined individual double-wall carbon nanotubes. *Nano Res.* **2014**, *7*, 1548−1555.

(39) Liu, K.; Hong, X.; Choi, S.; Jin, C.; Capaz, R. B.; Kim, J.; Wang, W.; Bai, X.; Louie, S. G.; Wang, E.; Wang, F. Systematic determination of absolute absorption cross-section of individual carbon nanotubes. *Proc. Natl. Acad. Sci. U. S. A.* **2014**, *111*, 7564−7569.

(40) Cronin, S. B.; Yin, Y.; Walsh, A.; Capaz, R. B.; Stolyarov, A.; Tangney, P.; Cohen, M. L.; Louie, S. G.; Swan, A. K.; Unlu, M. S.; Goldberg, B. B.; Tinkham, M. Temperature dependence of the optical transition energies of carbon nanotubes: The role of electron-phonon coupling and thermal expansion. *Phys. Rev. Lett.* **2006**, *96*, 127403.

(41) May, P.; Telg, H.; Zhong, G. F.; Robertson, J.; Thomsen, C.; Maultzsch, J. Observation of excitonic effects in metallic single-walled carbon nanotubes. *Phys. Rev. B: Condens. Matter Mater. Phys.* **2010**, *82*, 195412.

(42) Walsh, A. G.; Vamivakas, A. N.; Yin, Y.; Cronin, S. B.; Unlu, M. S.; Goldberg, B. B.; Swan, A. K. Screening of excitons in single, suspended carbon nanotubes. *Nano Lett.* **2007**, *7*, 1485.

(43) Chiashi, S.; Kono, K.; Matsumoto, D.; Shitaba, J.; Homma, N.; Beniya, A.; Yamamoto, T.; Homma, Y. Adsorption effects on radial breathing mode of single-walled carbon nanotubes. *Phys. Rev. B: Condens. Matter Mater. Phys.* **2015**, *91*, 155415.

(44) Finnie, P.; Homma, Y.; Lefebvre, J. Band-gap shift transition in the photoluminescence of single-walled carbon nanotubes. *Phys. Rev. Lett.* **2005**, *94*, 247401.

(45) Araujo, P. T.; Pesce, P. B. C.; Dresselhaus, M. S.; Sato, K.; Saito, R.; Jorio, A. Resonance Raman spectroscopy of the radial breathing modes in carbon nanotubes. *Phys. E* **2010**, *42*, 1251−1261.

(46) Wang, F.; Dukovic, G.; Brus, L. E.; Heinz, T. F. Time-resolved fluorescence of carbon nanotubes and its implication for radiative lifetimes. *Phys. Rev. Lett.* **2004**, *92*, 177401.

(47) Srivastava, A.; Htoon, H.; Klimov, V. I.; Kono, J. Direct observation of dark excitons in individual carbon nanotubes: Inhomogeneity in the exchange splitting. *Phys. Rev. Lett.* **2008**, *101*, 087402.

https://dx.doi.org/10.1021/acs.jpclett.0c03320
J. Phys. Chem. Lett. 2020, 11, 10497−10503

Supporting Information

Electronic Raman Scattering in Suspended Semiconducting Carbon Nanotube

Yuecong Hu, Shaochuang Chen, Xin Cong, Sida Sun, Jiang-bin Wu, Daqi Zhang, Feng Yang, Juan Yang, Ping-Heng Tan, and Yan Li**

Keywords: electronic Raman scattering, single-walled carbon nanotubes, electronic structure, resonant Raman spectroscopy, chirality assignments

Error Analysis for ERS spectra

The total error in determining the uncertainty in transition energies by ERS features in a single spectrum is about ± 1 meV. This total error consists of three parts:

1. The spectral resolution is determined by the gratings and the focal length of the Raman spectrometer used to collect the ERS spectra. It is ~4 cm^{-1} around 532 nm and ~3 cm^{-1} around 785 nm using a JY LabRAM ARAMIS spectrometer (focal length: 460 mm) with a 300 grooves/mm grating. The error introduced by spectral resolution is ~0.5 meV.

2. The random noise typically contribute an error of ~0.2 meV by including the random noise in the fitting using an open-source software Fityk (http://fityk.nieto.pl/).

3. The spectral fitting errors are estimated by carrying out several independent runs of fitting with different initial parameters. All parameters are allowed to vary freely in the peak fitting

process. The magnitude of this error is affected by the ERS intensity as well as its overlapping with other phonon Raman bands. As a result, the spectral fitting error is ~1.3 meV.

Laser Heating Effect

A suspended (15,2) nanotube was intentionally heated with different powers of the 532 nm laser to reveal how temperature changes have affected both the ERS feature and the phonon peaks. Figure S1 shows the Raman spectra at the exactly same spot on this (15,2) nanotube at a lower laser power (0.92 mW) and a higher laser power (2.30 mW). The ERS feature show considerable redshift and all phonon peaks remain nearly unchanged at increased laser power. This redshifts in ERS can be explained by the thermal expansion of the nanotube and the consequently decreased transition energies.

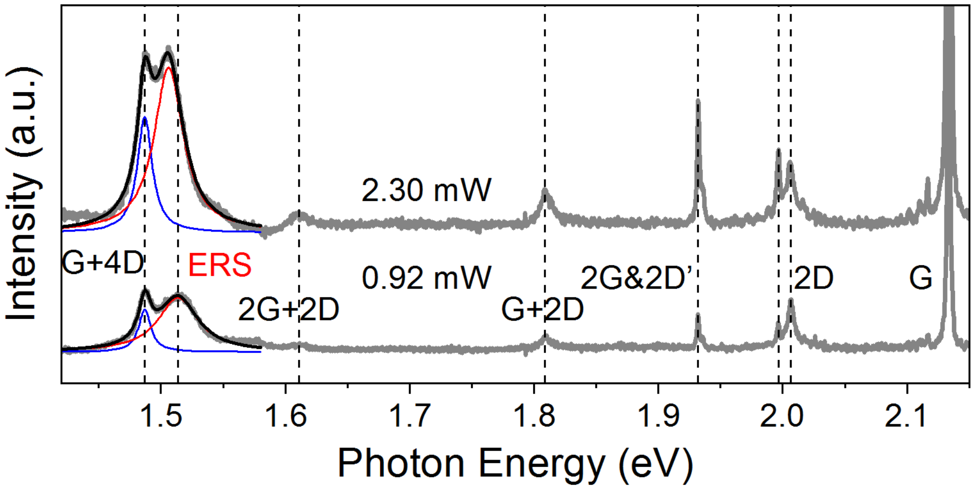

Figure S1. Raman spectra at the exactly same spot on a suspended (15,2) nanotube at two different powers of the 532 nm laser.

More ERS Data

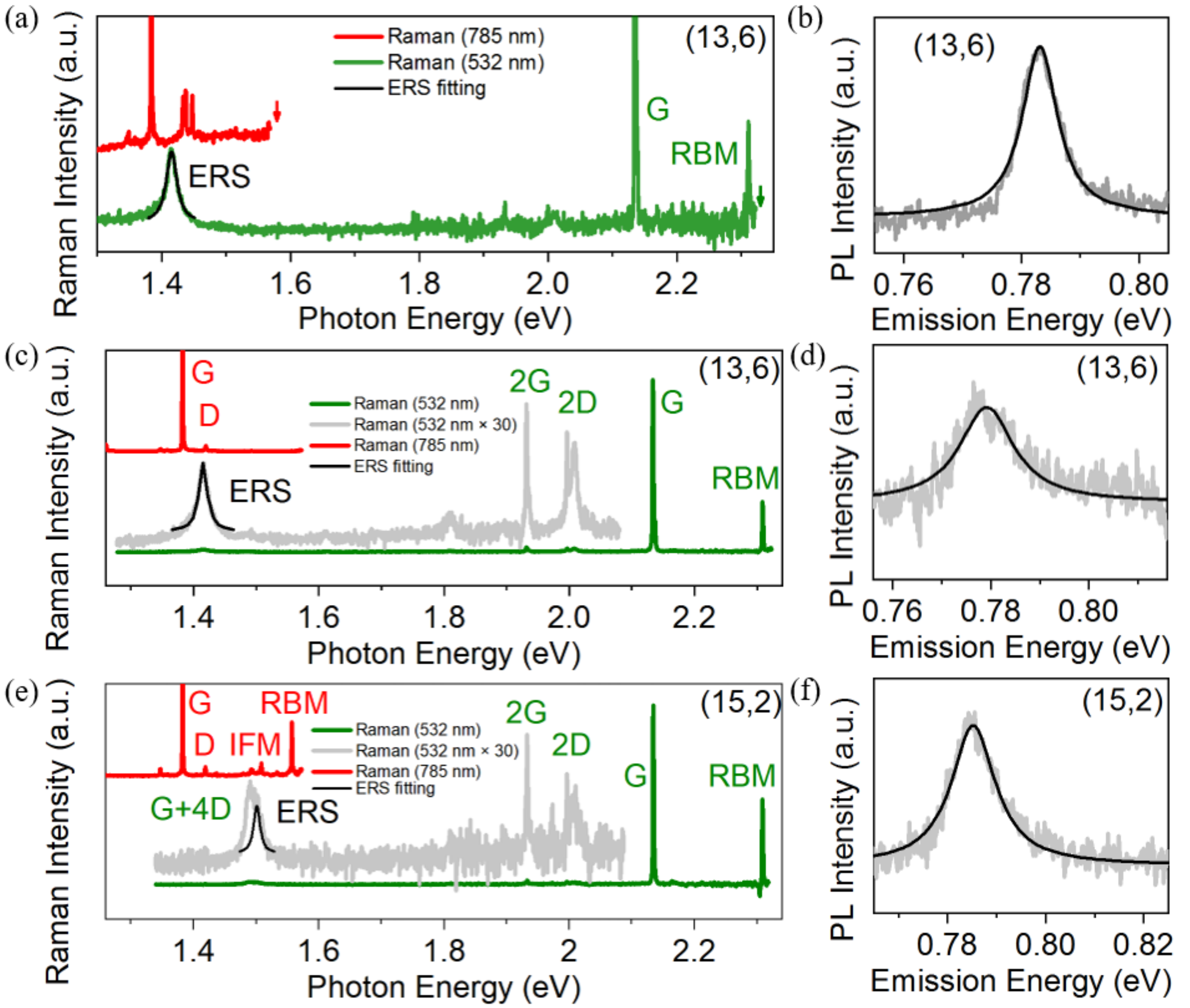

Figure S2. Additional Raman and ERS features (a, c, e) and PL spectra (b, d, f) of suspended tubes in the $2n+m = 32$ family at 532 (green) and 785 (red) nm excitations.

Table S1. The transition energies, ERS features, and PL peaks of the suspended chiral nanotubes in the $2n+m$ = 32 family. Altogether four (15,2), one (14,4), three (13,6), and one (12,8) nanotubes are observed.

(n,m)	S_{22}[a) [eV]	ERS Observed[b) [eV]	ΔS_{22} [eV]	S_{11}[a) [eV]	PL Observed[c) [eV]	ΔS_{11} [eV]
(15,2)	1.522	1.513	−0.009	0.803	0.799	−0.004
		1.506	-0.016		0.796	-0.007
		1.505	-0.017		0.800	-0.003
		1.501	−0.021		0.785	−0.018
(14,4)	1.485	1.470	−0.015	0.797	0.792	−0.005
(13,6)	1.431	1.415	−0.016	0.785	0.786	0.001
		1.415	−0.016		0.783	−0.002
		1.415	−0.016		0.780	−0.005
(12,8)	1.365	1.356	−0.009	0.769	0.774	0.005

a)Calculated using the (n,m) calculator on www.chem.pku.edu.cn/cnt_assign; b)ERS observed at 532 nm excitation (E_L = 2.330 eV); c)PL observed at 785 nm excitation (E_L = 1.579 eV).